Exploring the Flow Dynamics of MHD Hybrid Nanofluid over a Non-Flat Porous Surface Using Neural Network Approach

Himanshu Upreti[1,2], Alok Kumar Pandey[3,*] and Tanya Gupta[4]

[1] SoET, BML Munjal University, Gurugram, 122413, Haryana, India

[2] Center for Advanced Data and Computational Science, BML Munjal University, Gurugram, 122413, Haryana, India

[3] Department of Mathematics, Graphic Era (Deemed to be University), Dehradun, 248002, Uttarakhand, India

[4] Department of Mathematics, IAH, GLA University, Mathura, 281406, Uttar Pradesh, India

INFORMATION

Keywords:
Levenberg-Marquardt algorithm
magnetohydrodynamics flow
neural network
slip mechanism
variable thermal conductivity

DOI: 10.23967/j.rimni.2025.10.64380

SCIPEDIA Revista Internacional de Métodos Numéricos para Cálculo y Diseño en Ingeniería

RIMNI Revista Internacional Métodos numéricos para cálculo y diseño en ingeniería

Exploring the Flow Dynamics of MHD Hybrid Nanofluid over a Non-Flat Porous Surface Using Neural Network Approach

Himanshu Upreti[1,2], **Alok Kumar Pandey**[3,*] **and Tanya Gupta**[4]

[1]SoET, BML Munjal University, Gurugram, 122413, Haryana, India

[2]Center for Advanced Data and Computational Science, BML Munjal University, Gurugram, 122413, Haryana, India

[3]Department of Mathematics, Graphic Era (Deemed to be University), Dehradun, 248002, Uttarakhand, India

[4]Department of Mathematics, IAH, GLA University, Mathura, 281406, Uttar Pradesh, India

ABSTRACT

The current work examined the heat transfer performance of TiO_2-Al_2O_3/kerosene oil flowing over a permeable non-flat plate. The energy equation is modeled using Fourier's law, and heating is supported by Joule heating and nonlinear thermal radiation. Moreover, the momentum equation is extended with mixed convection, magnetic field, and porous medium. We applied an artificial neural network (ANN) to the data obtained from the bvp4c solver to show the significance of AI techniques in predicting skin friction coefficient (SFC) and local Nusselt number (LNN) values. The ANN is developed with the Levenberg-Marquardt backpropagation algorithm to predict the values precisely, and its significance is assessed in terms of mean square error (MSE) between values obtained by the bvp4c solver and the predicted value neural network. The outcomes revealed that the heat transfer rate decayed with the rise in variable thermal conductivity. Moreover, when increasing the magnitude of the mixed convection parameter, the fluid velocity constantly increases.

OPEN ACCESS

Received: 13/02/2025

Accepted: 11/04/2025

Published: 30/05/2025

DOI
10.23967/j.rimni.2025.10.64380

Keywords:
Levenberg-Marquardt algorithm
magnetohydrodynamics flow
neural network
slip mechanism
variable thermal conductivity

Nomenclature

B_0	Magnetic field strength (T)
C_{fx}	Skin friction coefficient
C_P	Specific heat (J kg^{-1} K^{-1})
Ec	Eckert number
f	Dimensionless velocity
g	Dimensionless velocity
Gr_x	Local Grashof number
k	Permeability
m	Velocity power index

*Correspondence: Alok Kumar Pandey (mr.alokpandey1@gmail.com). This is an article distributed under the terms of the Creative Commons BY-NC-SA license

Mn	Magnetic parameter
Nu_x	Local Nusselt number
Pr	Prandtl number
Ra	Radiation parameter
Re_x	Local Reynolds number
T	Temperature (K)
T_s	Surface temperature (K)
u_1, u_2	Velocity components along x- and y-axes, respectively (m s^{-1})
U_s	Stretching sheet velocity (m/s)

Greek Symbols

β_T	Thermal expansion coefficient (K^{-1})
γ	Slip coefficient
δ	Thickness parameter
ε	Thermal conductivity variation parameter
ρ	Density (kg m^{-3})
$\lambda_a, \lambda_b, \lambda_c, \lambda_d, \lambda_e, \lambda_f$	Dimensionless constants
χ	Porosity parameter
μ	Dynamic viscosity (kg m^{-1} s^{-1})
σ	Electrical conductivity (Ω^{-1} m^{-1})
ν	Kinematic viscosity (m^2 s^{-1})
ς	Mixed convection parameter
Θ	Dimensionless temperature
θ	Dimensionless temperature
ξ, η	Similarity variables
κ	Thermal conductivity ($Wm^{-1}K^{-1}$)
σ	Electrical conductivity ($\Omega^{-1}m^{-1}$)
σ^*	Stefan-Boltzmann constant ($Wm^{-2}K^{-4}$)
ψ	Stream function
ω	Velocity slip parameter
θ_s	Temperature ratio parameter
φ	Volume fraction of nanoparticles (%)

Subscript

∞	Ambient condition
f	Base fluid
hf	Hybrid nanofluid
nf	Nanofluid

Superscript

'	Derivative w.r.t η

Abbreviations

AI	Artificial intelligence
ANN	Artificial neural network
BL	Boundary layer

MHD	Magnetohydrodynamics
MSE	Mean square error
LNN	Local Nusselt number
SFC	Skin friction coefficient
SS	Stretching sheet
TR	Thermal radiation
NN	Neural network
bvp	Boundary value problem

1 Introduction

The key concept of fluid flow over a flat plate is versatile and has favorable applications in various domains. The applications can be seen in thermal protection systems for spacecraft, streamlined designing of automobiles, cooling fins, solar panels, wind turbines, and many more. The performance of these systems is influenced by liquid or air flow over them. To optimize the presentation of the systems involving flat plates, the flow behavior over the plate must be studied. Turkyilmazoglu et al. [1] presented an analytical work to study the transient free convection flow along with isothermal and isoflux boundary conditions over the flat plate. They analyzed the flow for different nanofluids under the radiation effect. They disclosed that the radiation effect increases skin friction and decreases the heat transfer rate. Hatami et al. [2] analyzed the MHD nanofluid flow over a horizontal plate in which forced convection was considered. They applied the homotopy analysis method (HAM) and exposed that HAM can be a powerful technique for obtaining the solution. Ahmadi et al. [3] discussed the differential transformation method to analyze the unsteady flow over a stretching flat plate. They disclosed that the unsteadiness parameter plays a vital role in flow phenomena. They discovered the direct relationship between the unsteadiness parameter and the velocity of the nanofluid. Later, Das et al. [4] worked on unsteady flow over a porous flat plate, considering it in a rotating frame. They found that the heat transfer rate is reduced with the rise in rotation parameter. They also revealed the existence of a thin boundary layer in the proximity of the plate for a long time. Irfan et al. [5] analyzed the Carreau nanofluid flow in the presence of MHD and nonlinear radiation with gyrotactic microorganisms. They analyzed the thermophoresis and Brownian factors in their study. Shahlaei et al. [6] investigated the MHD radiative nanofluid over a stretching surface under the influence of Joule heating. They studied the complete flow under couple stress. They disclosed a direct relation of Nusselt number with the radiation and an inverse relation between skin friction and couple stress. Verma et al. [7] presented an experimental work to analyze the energy proficiency of solar collectors. This analysis was carried out for different nanoparticles in water-based nanofluids. They showed an enhancement of exergy effectiveness for multi-wall carbon nanotubes (CNTs) by 29.32%. Bazdidi-Tehrani et al. [8] have numerically investigated the nanofluid flow through a ribbed flat-plate solar collector. The study was performed for the three-dimensional flow through the plain and ribbed duct for different Reynolds numbers. It was demonstrated that the efficiency of the solar collector is proportional to the volume fraction of nanoparticles. Also, in a comparison analysis, it was found that ribbed ducts are 10% more efficient than plain ducts. In the continuation of work on solar collectors, Tong et al. [9] did an experimental analysis of the energy and exergy of solar collectors. It was disclosed that Al_2O_3-H_2O and CuO-H_2O could significantly enhance the efficiency of solar collectors compared to water. Saffarian et al. [10] investigated the effect of different flow path shapes (spiral, wavy U-shaped) on a solar collector in its heat transfer enhancement using nanofluids. It was concluded that spiral and wavy pipes can enhance the Nusselt number. Specifically, wavy pipes and CuO-H_2O can upsurge the heat transfer coefficient to 72.25% at a 4% volume fraction. Khademi et al. [11] analyzed

the fluid past a porous plate under the consequence of the transverse magnetic field. The model was simulated using the Differential Quadrature Method. Wahid et al. [12] explored the convective flow of a hybrid nanofluid over a vertical plate in the proximity of the radiation effect. It was disclosed that the heat transfer can be improved by mixed convection for less concentration of copper and high values of radiation parameter. Later, many researchers worked on flat plates that can be referenced as Khan et al. [13], Thakur et al. [14], Mandal et al. [15], Elsaid et al. [16], and Bartwal et al. [17].

Artificial Neural Network (ANN) play a vital role in studying the heat transfer and thermal performance of systems, reducing the complexity of the computation. It uses artificial neurons as the units. These models consist of interconnected neurons for data processing and thermal performance analysis. In light of this, Ermis et al. [18] projected a FFB (Feed-Forward Back) propagation ANN algorithm to simulate the heat transfer. They found that the ANN results were more precise than the approximate solution. Later, Popescu et al. [19] used the ANN approach to discuss the possibility of controlling induction driving. They discussed the concept and application of multilayer perceptron, which is a type of neural network using a backpropagation algorithm. Balachandar et al. [20] used the ANN approach to analyze the heat transfer performance of a hollow cylindrical pin fin array considering its base plate rectangular. The Genetic Algorithm was additionally applied on NN to optimize the pin fin parameters for maximum heat transfer. They disclosed that hollow cylinders provide improved heat transfer in comparison to solid cylinders. Hamdan et al. [21] developed a model consisting of a flat plate, solar collector, and absorbing plate. They applied the nonlinear autoregressive exogenous (NARX) ANN model to analyze the heat transfer. It was disclosed that the NARX model provides brilliant accuracy in evaluating the mean temperature of the flat plate collector. Verma et al. [22] presented a comparative analysis of heat transfer of heat exchanger with or without helical ribs. They implemented an ANN to evaluate the performance factors of the heat exchanger. Naphon et al. [23] examined the heat transfer of jet impingement nanofluid flow in the micro-channel. They used the LMB "Levenberg-Marquardt Backward" propagation ANN algorithm to obtain the optimal solution. This method presented a precise prediction of the data. Sharma et al. [24] applied the Levenberg-Marquardt NN scheme to study the ternary hybrid nanofluid flow within parallel plates in the proximity of the Nield boundary condition. After conducting an experimental investigation, Alklaibi et al. [25] provided ANN predictions for the hybrid nanofluids' heat transport and friction factor. Reddy et al. [26] examined the hybrid dusty Eyring-Powell nanofluid flow using bvp4c solver. The ANN approach was applied using the Levenberg-Marquard algorithm for prediction. It was concluded that ANN does not need linearization and requires less processing power with fast convergence. Their research demonstrates the capability of artificial neural networks to effectively predict hybrid nanofluids in thermal systems. Some more work on ANN can be seen in the literature of Ferdows et al. [27], Raja et al. [28], and Kumar et al. [29].

Research in heat transfer is inevitably advancing, concentrating on enhancing the efficiency of energy systems, creating material with superior thermal conductivity (TC), and tackling difficulties associated with climate change, including urban heat islands and renewable energy harvesting. Examining heat transfer is crucial for enhancing systems in various industries and developing sustainable technologies. Mandal et al. [30] simulated the MHD hybrid nanofluid flow over a W-shaped cavity with the aid of mixed convection for analyzing the heat transfer. They applied the finite volume method for the simulations. Pantokratoras et al. [31] studied Sakiadis flow incorporating NRTR "nonlinear Rosseland thermal radiation", elucidating the influence of radiation on BL behavior in a flowing fluid over a flat plate. Fang et al. [32] analyzed the flow behavior of fluid over SS with variable thickness. They concluded that the nonlinear phenomena are offered by SS "stretching sheets" with variable thickness compared to flat sheets. Khader et al. [33] considered slip velocity on the over a nonlinear

stretching sheet. They used the finite difference method (FDM) for simulation. Elbashbeshy et al. [34] inquired about the consequences of TR on the flow and heat transfer of nanofluids across a moving surface characterized by variable thickness and nonlinear velocity. The findings point out that radiation significantly increase the thickness of the thermal BL, indicating that radiation improves heat transfer in systems characterized by varying surface properties. Acharya et al. [35] focused on the magnetized flow in the proximity of nonlinear TR across permeable surfaces. They used the homotopy perturbation method and concluded the enhanced heat transfer through the radiation parameter. Gangadhar et al. [36] considered electro-magnetohydrodynamics (EMHD) flow over a Riga plate in which the radiative second-grade nanofluid, along with convective heating, was taken into account. They applied the Runge-Kutta-Fehlberg method for the simulation. Many more researchers analyzed the heat transfer phenomena that can be seen in the literature: Zainal et al. [37], Masood et al. [38], Sandeep et al. [39], Waqas et al. [40], and Vijay et al. [41].

In this work, the heat transfer performance in magnetized hybrid nanofluid flow via non-flat plate using the NN model is examined. Moreover, impacts of magnetic field, permeability, power law index variable, mixed convection, nonlinear TR, and slip velocity on flow and temperature fields are revealed. The bvp4c solver solved the existing equations present in the flow model, and the results are validated graphically. The purpose of this study is to fill the research gap by examining the heat transfer phenomenon in hybrid nanofluid (TiO_2-Al_2O_3/kerosene oil) flow through a permeable stretching sheet, which was not analyzed by the above literature. The key novelties of this work are:

- Examine the performance of heat transfer in TiO_2-Al_2O_3/kerosene oil hybrid nanofluid flow over a non-flat plate, which is significant for thermal engineering applications
- Inspect the simultaneous impact of mixed convection, permeability, and slip velocity on velocity and temperature fields of existing fluids since it is crucial to optimize heat transfer in industrial applications such as microfluidic devices and thermal insulation technologies.
- Observe the impact of magnetohydrodynamics and Joule heating to analyze heat transfer and fluid flow. These effects enable precise flow control and temperature distributions in conductive fluids
- Artificial neural network technique is used on the data generated from the bvp4c solver to display the significance of AI techniques in forecasting SFC and LNN values.
- The ANN is developed with the Levenberg-Marquardt backpropagation algorithm to foresee the values, and its importance is assessed in the context of mean square error between values attained by bvp4c solver and forecast value neural network. This approach minimizes the computational costs and accelerates simulations. Additionally, it can make real-time predictions for nonlinear bvp.

Real-life applications and significance of the present work are:

- This study uses the MHD hybrid nanofluid flow, which can be used in nuclear reactors, cooling systems, and biomedical domains. For instance, in cancer treatment, cancer cells can be destroyed using magnetic nanoparticles.
- Porous media, along with the variable thermal conductivity, are vital in energy storage systems, as in solar energy collectors, to manage high heat load.
- This study will be helpful in studying the domains where high-temperature environments (combustion chambers, industrial furnaces) are present as it involves nonlinear thermal radiation.

2 Problem Formulation

Consider a plate placed along x-axis, i.e., $y = 0$ in the rectangular coordinate system, as illustrated in Fig. 1. The surface of the plate is non-flat with varying thickness described as $y = \varsigma(x + c)^{\frac{1-m}{2}}$, and it changes with the distance from the origin. The surface of the plate is porous and maintained at constant wall temperature T_s (K). The porous medium is assumed to be homogeneous and isotropic, and flow is considered within the Darcy regime, neglecting the Forchheimer correction term, which accounts for non-Darcian effects at high velocities.

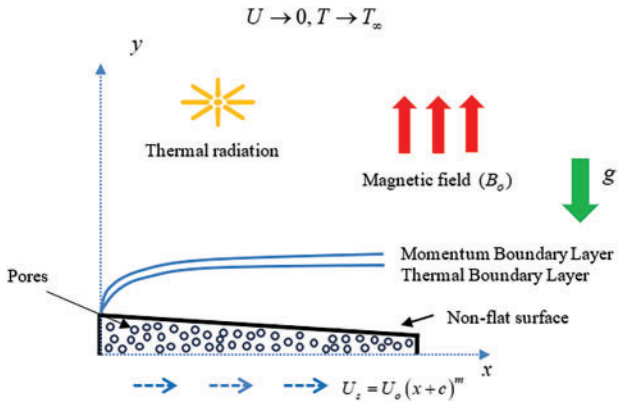

Figure 1: Schematic representation of the flow problem

Consider a two-dimensional, time-independent, and viscous flow of hybrid nanofluid (hf) over the aforementioned plate moving along x-axis with velocity $U_s = U_0(x+c)^m$. The flow is buoyancy driven and modelled using the Boussinesq approximation. A uniform strength magnetic field B_o (T) applied along y-axis, i.e., normal to the plate. The induced magnetic field is neglected due to the assumptions of a low magnetic Reynolds number. The mechanism of heat transfer is modelled using Fourier's law and is supported by non-linear thermal radiation, as well as the heat generated due to the magnetic field (Ohmic heating) and friction existing between the layers (viscous dissipation). The local thermal equilibrium (LTE) assumption is considered, meaning the nanofluid and solid matrix in the porous medium are at the same temperature. Further, it is assumed that the thermal conductivity (TC) of hf is temperature dependent (see Eq. (5)), and the surface effect of slip velocity is also considered.

The hybrid nanofluid considered here is prepared by dispersing TiO_2 nanoparticles in kerosene oil to prepare mono-nanofluid and then adding Al_2O_3 nanoparticles into TiO_2/kerosene oil. The thermophysical properties (TP), as well as the relations used to compute effective TP, are presented in Tables 1 and 2, respectively.

Table 1: Properties of kerosene oil and nanoparticles, i.e., TiO_2 and Al_2O_3 [9,42]

	Kerosene Oil	TiO_2	Al_2O_3
μ $\left(\text{kg}\cdot\text{m}^{-1}\cdot\text{s}^{-1}\right)$	1.64E−3	-	-
ρ $\left(\text{kg}\cdot\text{m}^{-3}\right)$	783	4250	3970
C_p $\left(\text{J}\cdot\text{kg}^{-1}\cdot\text{K}\right)$	2090	686.2	765
σ $\left(\text{S}\cdot\text{m}^{-1}\right)$	5E−11	1E−6	1E−10

(Continued)

Table 1 (continued)

	Kerosene Oil	TiO_2	Al_2O_3
$k\ (\mathrm{W \cdot m^{-1} \cdot K})$	0.145	8.9538	40
$\beta\ (\mathrm{K^{-1}})$	9.9E−4	0.9E−5	0.85E−5

Table 2: Models to compute the thermophysical properties of hybrid nanofluid [42]

$$\mu_{hf} = \frac{1}{\left(1-\varphi_{TiO_2}\right)^{2.5}\left(1-\varphi_{Al_2O_3}\right)^{2.5}}\mu_f$$

$$\rho_{hf} = \left(1-\varphi_{Al_2O_3}\right)\left[\left(1-\varphi_{TiO_2}\right)\rho_f + \varphi_{TiO_2}\rho_{TiO_2}\right] + \varphi_{Al_2O_3}\rho_{Al_2O_3}$$

$$\frac{k_{hf}}{k_f} = \frac{k_{hf}}{k_{nf}} \times \frac{k_{nf}}{k_f},$$

$$where\ \frac{k_{hf}}{k_{nf}} = \frac{k_{Al_2O_3} + 2k_{nf} - 2\varphi_{Al_2O_3}\left(k_{nf} - k_{Al_2O_3}\right)}{k_{Al_2O_3} + 2k_{nf} + \varphi_{Al_2O_3}\left(k_{nf} - k_{Al_2O_3}\right)}, \frac{k_{nf}}{k_f} = \frac{k_{TiO_2} + 2k_f - 2\varphi_{TiO_2}\left(k_f - k_{TiO_2}\right)}{k_{TiO_2} + 2k_f + \varphi_{TiO_2}\left(k_f - k_{TiO_2}\right)}$$

$$\frac{\sigma_{hf}}{\sigma_f} = \frac{\sigma_{hf}}{\sigma_{nf}} \times \frac{\sigma_{nf}}{\sigma_f},$$

$$where\ \frac{\sigma_{hf}}{\sigma_{nf}} = \frac{\sigma_{Al_2O_3} + 2\sigma_{nf} - 2\varphi_{Al_2O_3}\left(\sigma_{nf} - \sigma_{Al_2O_3}\right)}{\sigma_{Al_2O_3} + 2\sigma_{nf} + \varphi_{Al_2O_3}\left(\sigma_{nf} - \sigma_{Al_2O_3}\right)}, \frac{\sigma_{nf}}{\sigma_f} = \frac{\sigma_{TiO_2} + 2\sigma_f - 2\varphi_{TiO_2}\left(\sigma_f - \sigma_{TiO_2}\right)}{\sigma_{TiO_2} + 2\sigma_f + \varphi_{TiO_2}\left(\sigma_f - \sigma_{TiO_2}\right)}$$

$$(\rho\beta_T)_{hf} = \left(1-\varphi_{Al_2O_3}\right)\left\{\left(1-\varphi_{TiO_2}\right)(\rho\beta_T)_f + \varphi_{TiO_2}(\rho\beta_T)_{TiO_2}\right\} + \varphi_{Al_2O_3}(\rho\beta_T)_{Al_2O_3}$$

$$(\rho C_P)_{hf} = \left(1-\varphi_{Al_2O_3}\right)\left\{\left(1-\varphi_{TiO_2}\right)(\rho C_P)_f + \varphi_{TiO_2}(\rho C_P)_{TiO_2}\right\} + \varphi_{Al_2O_3}(\rho C_P)_{Al_2O_3}$$

Based on the above-stated conventions and utilizing the boundary layer approximations, the equations governing the fluid flow are modelled as [4,32,35]:

$$\frac{\partial u_1}{\partial x} + \frac{\partial u_2}{\partial y} = 0, \tag{1}$$

$$\rho_{hf}\left(u_1\frac{\partial u_1}{\partial x} + u_2\frac{\partial u_1}{\partial y}\right) = \mu_{hf}\frac{\partial}{\partial y}\left(\frac{\partial u_1}{\partial y}\right) - \sigma_{hf}B_o^2 u_1 - \mu_{hf}\frac{u_1}{k} + g\left(\rho\beta_T\right)_{hf}\left(T - T_\infty\right), \tag{2}$$

$$(\rho C_P)_{hf}\left(u_1\frac{\partial T}{\partial x} + u_2\frac{\partial T}{\partial y}\right) = \frac{\partial}{\partial y}\left(\kappa_{hf}(T)\frac{\partial T}{\partial y}\right) + \sigma_{hf}B_o{}^2\left(u_1\right)^2 + \mu_{hf}\left(\frac{\partial u_1}{\partial y}\right)^2 + \frac{16\sigma^*}{3k^*}\frac{\partial}{\partial y}\left(T^3\frac{\partial T}{\partial y}\right), \tag{3}$$

with the following boundary conditions [33]:

$$\left.\begin{aligned} &u_1(x, y = \varsigma(x+c)^{0.5(1-m)}) = U_s + \gamma\frac{\partial u_1}{\partial y},\ u_2(x, y = \varsigma(x+c)^{0.5(1-m)}) = 0, \\ &T(x, y = \varsigma(x+c)^{0.5(1-m)}) = T_s, u_1(x, y \to \infty) \to 0,\ T(x, y \to \infty) \to T_\infty. \end{aligned}\right\} \tag{4}$$

The temperature dependent TC of hf is defined as [15]:

$$\kappa_{hf}(T) = \kappa_f(1 + \varepsilon\theta)\frac{\kappa_{hf}}{\kappa_f} \tag{5}$$

The symbols shown above referred to, u_1, u_2 velocity components along x- and y-axes, ρ_{hf} hybrid nanofluid density, μ_{hf} dynamic viscosity of hf, σ_{hf} electrical conductivity of hf, B_o magnetic field strength, k permeability of the porous medium, β_T thermal expansion coefficient, C_P specific heat, T temperature, T_s is surface temperature, T_∞ is ambient fluid temperature, κ_{hf} hybrid nanofluid TC, σ^* Stefan-Boltzmann constant, k^* is mean absorption coefficient, ς surface shape function, c is constant, γ is slip coefficient, m is velocity power index, and ε is TC variation parameter, respectively. The subscript hf, f and ∞ stands for hybrid nanofluid, base fluid, and ambient conditions, respectively.

To solve the Eqs. (1)–(3), it is necessary to reduce them to non-dimensional ordinary differential equations (ODEs); this is accomplished via the similarity transformations [33]. The stream function ψ is defined such that $u_1 = \frac{\partial \psi}{\partial y}$, $u_2 = -\frac{\partial \psi}{\partial x}$. The similarity variable is denoted by ξ, and the functions $g'(\xi), \Theta(\xi)$ are dimensionless quantities representing the primary flow velocity and temperature profiles, respectively.

$$\left.\begin{aligned} &\psi = \left(\left(\frac{2}{m+1}\right)\upsilon_f U_0 (x+c)^{(m+1)} g(\xi)\right)^{0.5}, \ \xi = \left(\frac{m+1}{2}\frac{U_0}{\upsilon_f}(x+c)^{m-1}\right)^{0.5} y, \\ &u_1 = U_0 (x+c)^m g'(\xi), \ u_2 = -\left(\frac{m+1}{2}\upsilon_f U_0 (x+c)^{m-1}\right)^{0.5}\left[g(\xi) + \xi\frac{m-1}{m+1}g'(\xi)\right], \\ &\Theta(\xi) = \frac{T - T_S}{T_S - T_\infty}. \end{aligned}\right\} \tag{6}$$

On applying Eq. (6), Eq. (1) is satisfied identically, and Eqs. (2) and (3) along with Eq. (4) reduced into the following forms:

$$\lambda_a\left(g''' - \frac{2m}{m+1}\chi g'\right) + \lambda_b\left(gg'' - \frac{2}{m+1}g'^2\right) - \frac{2m}{m+1}Mn\lambda_c g' + \lambda_d \zeta\Theta = 0, \tag{7}$$

$$\begin{aligned} &\lambda_f\left[(1+\varepsilon\Theta)\Theta'' + \varepsilon\Theta'^2\right] + Ra\left(1+\Theta\left(\theta_s - 1\right)\right)^2\left[\Theta'' + \left(\theta_s - 1\right)\left[\Theta\Theta'' + 3\Theta'^2\right]\right] \\ &\quad + Pr\left[Ec\left(\lambda_a g''^2 + 2\left(m+1\right)^{-1}\lambda_c Mng'^2\right) + \lambda_e g\Theta'\right] = 0. \end{aligned} \tag{8}$$

Boundary conditions:

$$\left.\begin{aligned} &g(\delta) = \delta\frac{(1-m)}{(1+m)}, g'(\delta) = 1 + \omega g''(\delta), \Theta(\delta) = 1 \text{ at } \xi = \delta\left(= \varsigma\sqrt{\frac{U_0(m+1)}{2\upsilon_f}}\right), \\ &g'(\delta) = 0, \ \Theta(\delta) = 0 \ as \ \xi \to \infty. \end{aligned}\right\} \tag{9}$$

Now, to convert the domain of integration from $[\delta, \infty)$ to $[0, \infty)$, invoke the following transformation:

$$\left.\begin{aligned} &g(\xi) = f(\eta)\ (= g(\xi - \delta)) \text{ and} \\ &\Theta(\xi) = \theta(\eta)\ (= \Theta(\xi - \delta)). \end{aligned}\right\} \tag{10}$$

Using Eq. (10), the following form of Eqs. (7)–(9) is obtained:

$$\lambda_a\left(f''' - \frac{2m}{m+1}\chi f'\right) + \lambda_b\left(ff'' - \frac{2}{m+1}f'^2\right) - \frac{2m}{m+1}Mn\lambda_c f' + \lambda_d\zeta\theta = 0 \tag{11}$$

$$\begin{aligned} &\lambda_f\left[(1+\varepsilon\theta)\theta'' + \varepsilon\theta'^2\right] + Ra\left(1+\theta\left(\theta_s - 1\right)\right)^2\left[\theta'' + \left(\theta_s - 1\right)\left[\theta\theta'' + 3\theta'^2\right]\right] \\ &\quad + Pr\left[Ec\left(\lambda_a f''^2 + 2\left(m+1\right)^{-1}\lambda_c Mnf'^2\right) + \lambda_e f\theta'\right] = 0, \end{aligned} \tag{12}$$

Boundary conditions:

$$\left.\begin{aligned} &f'(0) = 1 + \omega f''(0),\ f(0) = \delta\left(\frac{1-m}{1+m}\right),\ \theta(0) = 1,\\ &f'(\infty) = 0,\ \theta(\infty) = 0. \end{aligned}\right\} \tag{13}$$

The symbols appearing in the above-equations and boundary conditions are magnetic field parameter Mn, local Grashof number Gr_x, buoyancy parameter ζ, Prandtl number Pr, porosity parameter χ, local Reynolds number Re_x, radiation parameter Ra, temperature ratio θ_s, thickness parameter δ, velocity slip parameter ω, respectively, and are defined as:

$$\left.\begin{aligned} &Mn\left(=\frac{B_o^2\sigma_f}{\rho_f u_f}\right),\ Gr_x\left(=\frac{g\beta_T\left(T_S - T_\infty\right)(x+b)^3}{\upsilon_f^2}\right),\ \zeta\left(=\frac{Gr_x}{Re_x^2}\right), Pr\left(=\frac{\upsilon_f}{\alpha_f}\right),\\ &\chi\left(=\frac{\upsilon_f}{kU_0(x+b)^{m-1}}\right),\ Re_x\left(=\frac{U_s(x+b)}{\upsilon_f}\right), Ra\left(=\frac{16\sigma^* T_\infty^3}{3k^*\kappa_f}\right), \theta_s\left(=\frac{T_S}{T_\infty}\right)\\ &\delta\left(=\varsigma\sqrt{\frac{U_0(m+1)}{2\upsilon_f}}\right),\ \omega\left(=\sqrt{\frac{U_0(m+1)}{2\upsilon_f}}\right) \end{aligned}\right\}.$$

and, $\lambda_a\left(=\frac{\mu_{hf}}{\mu_f}\right)$, $\lambda_b\left(=\frac{\rho_{hf}}{\rho_f}\right)$, $\lambda_c\left(=\frac{\sigma_{hf}}{\sigma_f}\right)$, $\lambda_d\left(=\frac{(\rho\beta_T)_{hf}}{(\rho\beta_T)_f}\right)$, $\lambda_e\left(=\frac{(\rho C_p)_{hf}}{(\rho C_p)_f}\right)$, $\lambda_f\left(=\frac{\kappa_{hf}}{\kappa_f}\right)$ are the ratio of hybrid nanofluid to the kerosene oil.

The physical quantities are expressed as [25,26]:

$$C_f = \frac{\mu_{hf}}{\rho_f U_s}\left.\frac{\partial u_1}{\partial y}\right|_{y=\varsigma(x+c)^{\frac{1-m}{2}}}, \tag{14}$$

$$Nu = -\frac{(x+c)}{\kappa_\infty\left(T_s - T_\infty\right)}\left(\kappa_{hf}(T) + \frac{16\sigma^* T^3}{3k^*}\right)\left.\frac{\partial T}{\partial y}\right|_{y=\varsigma(x+c)^{\frac{1-m}{2}}}. \tag{15}$$

Using Eqs. (6) and Eq. (10), the dimension free form of SFC and LNN are:

$$C_{fx} = C_f Re_x^{1/2} = \lambda_a\left(\frac{2}{m+1}\right)^{-0.5} f''(0), \tag{16}$$

$$Nu_x = NuRe_x^{-1/2} = -\left[\lambda_f\left(1 + \varepsilon\theta\right) + Ra\left(1 + (\theta_s - 1)\right)^3\theta(0)\right]\theta'(0) \tag{17}$$

3 Solution Methodology

Over the past decades, numerous studies have been published that have used the bvp4c solver; Kierzenka et al. [43] were the first to solve equations using the bvp4c solver. Recently, this method was used by Irfan et al. [44] to simulate the radiative flow of Carreau nanofluid.

The bcp4c solver is based on a finite-difference collocation method, employing a three-stage Lobatto IIIa formula. The advantage of this method is its proficiency in dealing with complex boundary conditions and nonlinear problems. Additionally, its adaptive mesh refinement scheme adjusts the mesh for better accuracy for the sector in which the solution changes rapidly.

To solve the system using bvp4c, firstly, the set of ODEs are transformed to a set of first-order equations, and this is done by using these variables:

$$f = t_1,\ f' = t_2,\ f'' = t_3,\ \theta = t_4,\ \theta' = t_5, \tag{18}$$

Employing Eq. (18), Eqs. (12) and (13) are rewritten in the following form:

$$\left.\begin{aligned} tt_1 &= -\frac{\varpi_2}{\varpi_1}\left(t_1 * t_3 - (2-\beta) * t_2^2\right) + \frac{\varpi_2}{\varpi_1} * \beta * M * \varpi_3 * t_2 - \frac{\varpi_2}{\varpi_1} * \varpi_4 * \xi * t_4 + \varpi_4 * \beta * \lambda * t_2 \\ tt_2 &= \frac{-\varpi_6 * \varepsilon * t_5 * t_5 - 3Rd\left(1 + t_4 * (\theta_s - 1)\right)^2 (\theta_s - 1) * t_5 * t_5 - \varpi_1 * Ec * Pr * t_3 * t_3 + \beta * \varpi_3 * M * Ec * Pr * t_2 * t_2 + \varpi_5 * Pr * t_1 * t_5}{\left(\varpi_6 * (1 + \varepsilon * t_4) + Rd * \left(1 + t_4 * (\theta_s - 1)\right)^3\right)} \end{aligned}\right\} \tag{19}$$

with

$$\left.\begin{aligned} &t_2(a) = 1 + \omega * t_3(a),\ t_1(a) = \eta\left(\frac{1-m}{1+m}\right)[1 + \omega * t_3(a)],\ t_4(a) = 1 \\ &t_2(b) = 1, t_5(b) = 1 \end{aligned}\right\} \tag{20}$$

The bvp4c solver is accessed by the syntax described below:

"sol = bvp4c (@odeBVP, @odeBC, solinit, options)"

Here, the convergence is achieved when residual errors fall below 10^{-6} (relative) and 10^{-8} (absolute).

4 Code Validation

In order to confirm the approach that was followed, the authors verified their findings by comparing them to those of published research by Fang et al. [32], and Elbashbeshy et al. [34]. The outcomes are in good conciliation (see Table 3).

Table 3: Comparison of $-g''(0)$ values when $Pr = 1$, $Mn = 0 = Ec$, $Ra = 0$, $\omega = 0 = \theta_s$, and $\varphi_{TiO_2} = \varphi_{Al_2O_3} = 0$

α	n	Fang et al. [32]	Elbashbeshy et al. [34]	Present results
0.25	0	0.784 30	0.784 28	0.7848
0.50	0	0.957 60	0.957 64	0.9579

Further, the exact solution to the Eqs. (11) and (12) with the corresponding boundary conditions (13) is obtained considering the case when the pure-fluid ($\varphi = 0$) is flowing over a flat non-porous sheet, in the absence of the following terms, i.e., magnetic field, thermal radiation, and slip. Further, it is assumed that the TC of the fluid is invariant with temperature and there is no heating due to dissipation. Based on these, the Eqs. (11) and (12) along with Eq. (13) reduces to the following form:

$$f_{\eta\eta\eta} + f f_{\eta\eta} - \left(f_\eta\right) = 0, \tag{21}$$

$$\theta_{\eta\eta} + Prf\theta_\eta = 0. \tag{22}$$

boundary conditions:

$$\left.\begin{array}{l}\left(f_{\eta}\right)_{\eta=0}=1, f\left(\eta=0\right)=0, \theta\left(\eta=0\right)=1, \\ \left(f_{\eta}\right)_{\eta=\infty}=0, \theta\left(\eta=\infty\right)=0.\end{array}\right\} \tag{23}$$

Now, the exact solution to the above equations is obtained (Prasad et al. [45]):

$$f\left(\eta\right)=1-\exp\left(-\eta\right) \tag{24}$$

Using Eq. (24) in Eq. (22), and applying the reduction order method, the solution of the energy equation is:

$$\theta\left(\eta\right)=C_1-0.042^{*}C_2^{*}exp(-23.63^{*}\eta)^{*}exp(-23.63^{*}exp(-\eta))^{*}hypergeom(1.0,24.63,23.63^{*}exp(-\eta))$$

where C_1, C_2 are arbitrary constants, whose values are determined using Eq. (23).

Fig. 2a,b demonstrates the comparison of numerical results with that of exact results. The exact results are found for pure fluid in the absence of magnetic field, slip, thermal radiation, and Ohmic dissipation over a non-porous surface. Also, by taking thermal conductivity to be temperature independent. A good agreement is viewed with the exact results.

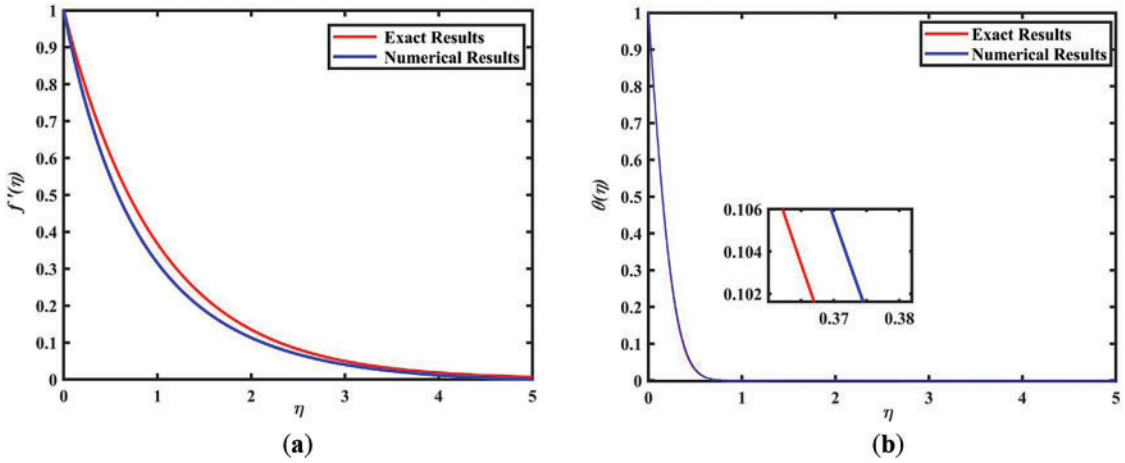

Figure 2: (a,b) Comparison of the numerical results with the exact solutions

5 Results and Discussion

This section presents the results of the study, including velocity and temperature profiles, SFC and LNN values, streamline plots, and LNN plot, along with their in-depth physical interpretation. Additionally, the present study also uses NN to predict the SFC and LNN for specific parameter values.

The parameters for which computation is done are magnetic (Mn), velocity slip (ω), porosity (χ), velocity power index (m), buoyancy parameter (ς), TC variation parameter (ε) and thickness parameter (δ), while other parameters such as Pr, Ra, Ec, θ_s are treated as constant. The computation is performed with a 5% volume fraction of each considered nanoparticle dispersed in the base fluid.

Table 4 describes the numerical values of the SFC and LNN for various parameters. It can be observed that SFC decreases on elevating the variable thickness, porosity, magnetic, and shape

parameters while increases with velocity slip and mixed convection parameter, whereas LNN decreases with variable thermal conductivity, magnetic and mixed convection parameter while increases with variable thickness, velocity slip, porosity and shape parameter. For a structured and systematic presentation, this section is organized under different subheadings, each discussing specific aspects of the study. The detailed discussion is presented as follows:

Table 4: Computed values of C_{fx} and Nu_x when $Pr = 23.63$, $\theta_s = 1.8$, $Ra = 2$, $Ec = 0.5$, and $\varphi_{TiO_2} = \varphi_{Al_2O_3} = 0.05$

ε	δ	ω	χ	ζ	Mn	m	SFC	LNN
0.25	0.25	0.5	2.5	0.02	2	0.25	−0.4028	4.5289
0.25	0.25	0.5	2.5	0.02	2	0.75	−0.7144	5.2893
0.25	0.25	0.5	2.5	0.02	2	1.25	−0.8879	5.3911
0.25	0.25	0.5	2.5	0.02	2	1.75	−1.0017	5.4313
0.25	0.25	0.5	2.5	0.02	0.2	0.5	−0.5345	7.4831
0.25	0.25	0.5	2.5	0.02	0.8	0.5	−0.5537	6.4418
0.25	0.25	0.5	2.5	0.02	1.4	0.5	−0.5707	5.6811
0.25	0.25	0.5	2.5	0.02	2	0.5	−0.586	5.1224
0.25	0.25	0.5	2.5	0.1	2	0.5	−0.5803	5.1128
0.25	0.25	0.5	2.5	0.4	2	0.5	−0.5591	5.0537
0.25	0.25	0.5	2.5	0.7	2	0.5	−0.5382	4.959
0.25	0.25	0.5	2.5	1	2	0.5	−0.5173	4.8308
0.25	0.25	0.5	0.5	0.02	2	0.5	−0.53	4.926
0.25	0.25	0.5	1	0.02	2	0.5	−0.546	5.0064
0.25	0.25	0.5	1.5	0.02	2	0.5	−0.5606	5.0617
0.25	0.25	0.5	2	0.02	2	0.5	−0.5738	5.0987
0.25	0.25	0.1	2.5	0.02	1	0.5	−0.9621	0.3636
0.25	0.25	0.4	2.5	0.02	1	0.5	−0.6235	5.4767
0.25	0.25	0.7	2.5	0.02	1	0.5	−0.4653	6.989
0.25	0.25	1.1	2.5	0.02	1	0.5	−0.3491	7.6852
0.25	0.01	0.5	2.5	0.02	2	0.5	−0.5669	0.5884
0.25	0.03	0.5	2.5	0.02	2	0.5	−0.5685	0.9185
0.25	0.05	0.5	2.5	0.02	2	0.5	−0.5701	1.2593
0.25	0.07	0.5	2.5	0.02	2	0.5	−0.5717	1.6099
0.1	0.25	0.5	2.5	0.02	2	0.5	−0.586	5.1365
0.2	0.25	0.5	2.5	0.02	2	0.5	−0.586	5.1265
0.3	0.25	0.5	2.5	0.02	2	0.5	−0.586	5.119
0.4	0.25	0.5	2.5	0.02	2	0.5	−0.586	5.1142

5.1 Neural Network (NN) Implementation and Analysis

In this work, the NN tool in MATLAB is used to develop an ANN model for prediction. The entire data consists of a total of 28 samples, the dataset was divided into training, verification, and testing subsets in the ratio of 80:10:10. The model involves input, hidden, and output layers. In the input layer, a total of 17 input parameters were utilized, and the model was trained on these parameters for the specific prediction of SFC and LNN values, which were generated using the applied bvp4c solver.

The ANN designed with the Levenberg-Marquardt backpropagation algorithm (LMBA) is shown in Fig. 3. The feed-forward NN was developed with training algorithm LMBA. The feed-forward network consists of two layers: (i) A hidden layer with 10 neurons using a PURELIN transfer function:

$$Hidden\ layer\ output\ \ (H) = f_{hidden}\,(W_{hidden}.X + b_{hidden}),$$

where $f_{hidden} = PURELIN\ \ (pure\ transfer\ function)$.

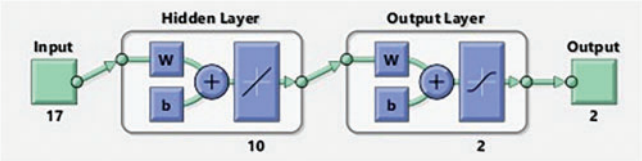

Figure 3: Neural network (NN) model

And (ii) an output layer with 2 neurons, corresponding to the predicted outputs (SFC and LNN), using a TANSIG transfer function:

$$Output\ layer\ output\ \left(\hat{Y}\right) = f_{output}\left(W_{output}.H + b_{output}\right),$$

where $f_{output} = TANSIG\ \ (hyperbolic\ tangent\ sigmoid\ transfer\ function)$.

To optimize the parameters (weight and bias) of the network, a gradient descent optimizer is utilized. The model's performance was estimated in terms of mean square error (MSE).

$$Mean\ square\ error\ \ (MSE) = \frac{1}{n}\sum_{i=1}^{n}(Y_i - \widehat{Y}_i)^2,$$

where n is the number of data points, Y_i observed values, and $\widehat{Y}_i$ is predicted value.

The network was trained for 14 iterations, achieving its best performance at the 8th iteration, where the validation performance was optimized. The least value of MSE for authentication is 0.0001367, see Fig. 4. For training, validation, and testing data, the value of R^2 are 0.99877, 0.99999, and 0.99601, respectively. The overall value of R^2 is 0.99841 obtained, see Fig. 5.

Table 5 shows the SFC and LNN values predicted via NN for distinct ε and δ, and their comparison with those obtained using bvp4c solver. It is observed that predicted and computed values are well matched.

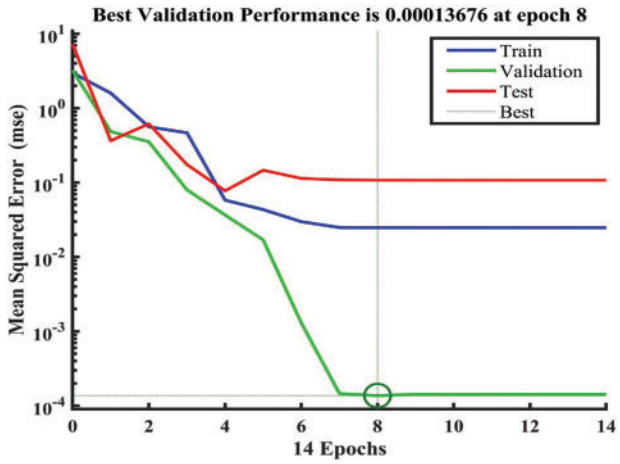

Figure 4: Training performance of developed NN model

Table 5: Comparison between the numerical and predicted value of SFC and LNN

			SFC			LNN		
m	***ε***	***δ***	**Using bvp4c**	**Predicted via NN**	**Error SFC**	**Using bvp4c**	**Predicted via NN**	**Error LNN**
0.5	0.25	0.05	−0.5701	−0.5703	0.00019947	1.2593	0.97085	0.28845
0.5	0.25	0.07	−0.5717	−0.57199	0.00029335	1.6099	1.1643	0.44561
0.5	0.1	0.25	−0.586	−0.58751	0.0015081	5.1365	5.1814	−0.04493
0.5	0.2	0.25	−0.586	−0.58751	0.0015081	5.1265	5.1814	−0.05493
0.5	0.3	0.25	−0.586	−0.58751	0.00158081	5.119	5.1814	−0.06243
0.5	0.4	0.25	−0.586	−0.58751	0.0015081	5.1142	5.1814	−0.06723

5.2 Streamlines

Streamlines are the visual representation of the paths that fluid particles follow for a specific moment. Flow patterns and fluid swirls can be observed. Here, the impact of the velocity power index (m) on streamlines is recorded considering the cases such as presence and absence of the magnetic field parameter and porosity parameter.

5.2.1 Impact of m When Mn = 0

Fig. 6a,c is sketched for two different values of shape parameters in the absence of a magnetic field. It is visualized that the streamlines become a little dense on increasing the shape parameter. These graphs show the flow pattern of fluid on account of shape parameter without any external force. It shows instant velocity changes at the denser part and leads to an increase in the vorticity, particularly in the region where the flow changes its direction promptly.

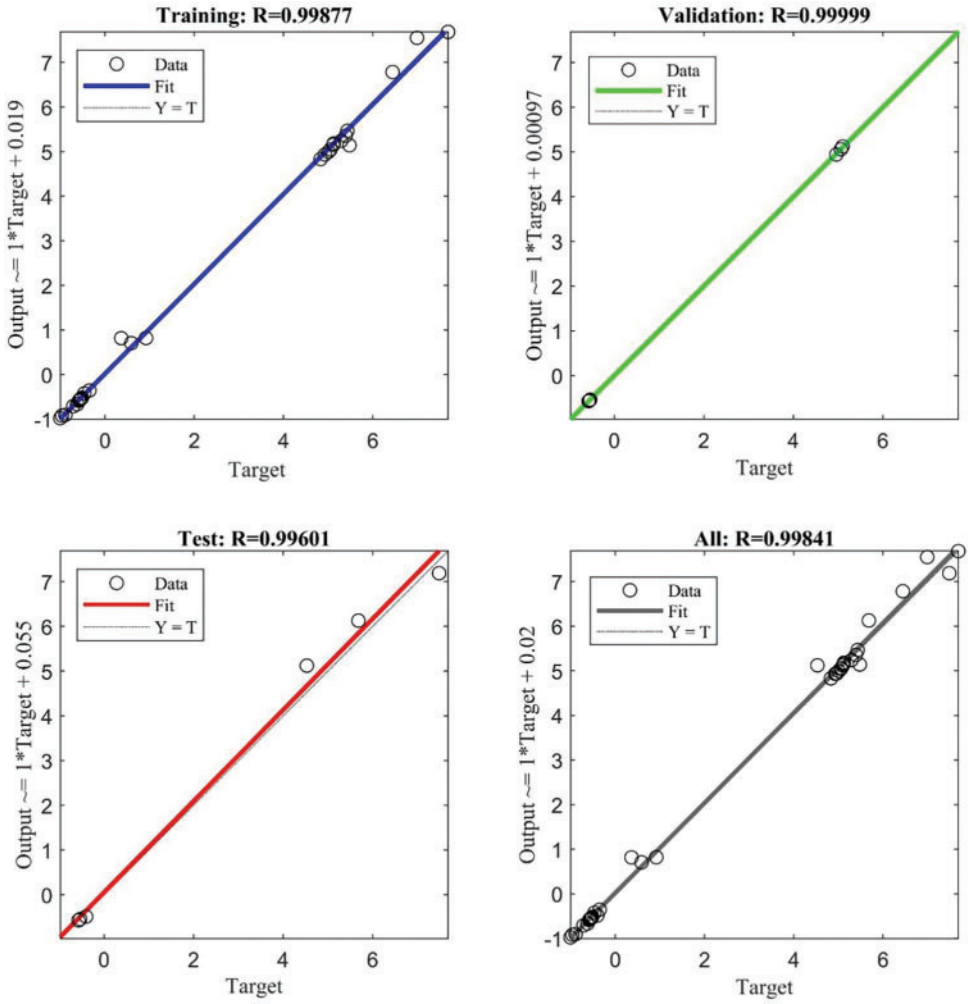

Figure 5: Regression values of developed NN model

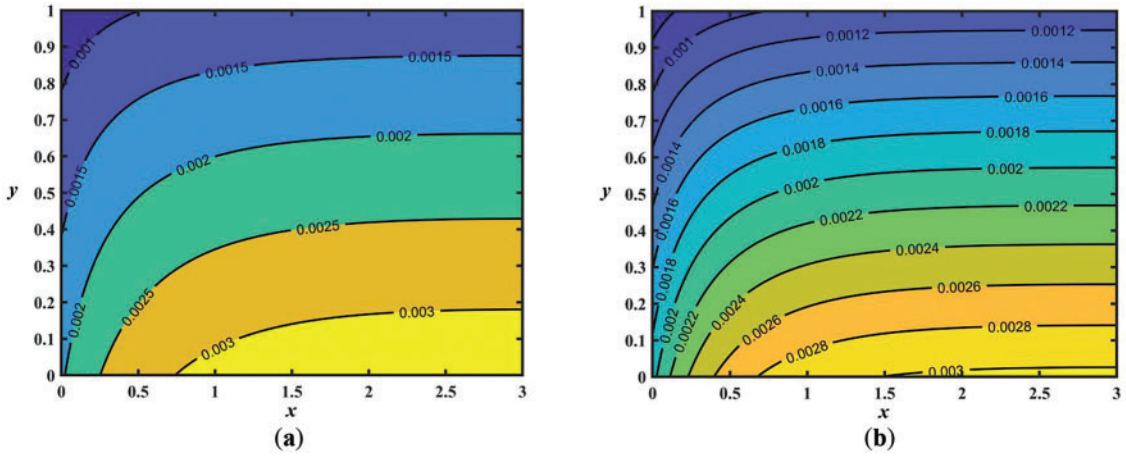

Figure 6: (Continued)

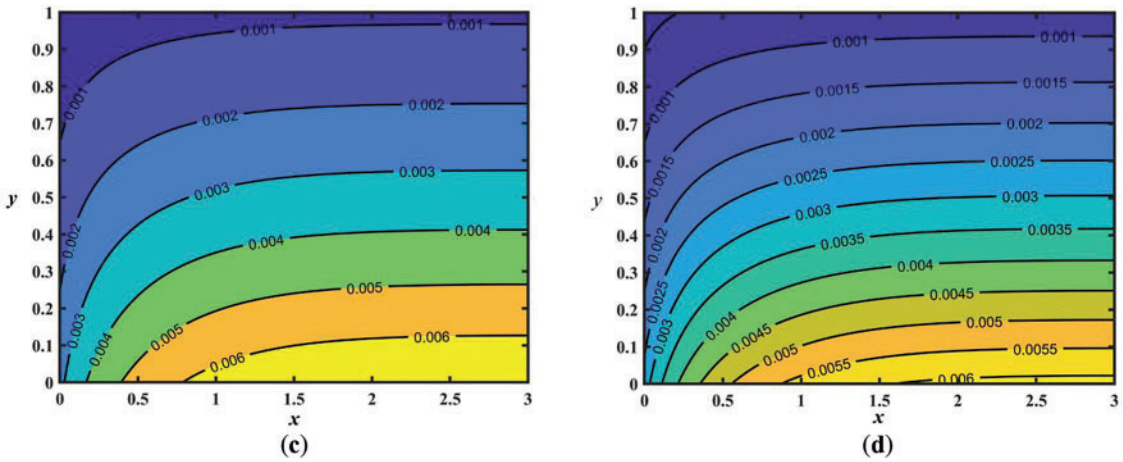

Figure 6: Effect of m and Mn on streamlines. (a) $m = 0.5$, $Mn = 0$; (b) $m = 0.5$, $Mn = 2$; (c) $m = 2$, $Mn = 0$; (d) $m = 2$, $Mn = 2$

5.2.2 Impact of m When Mn ≠ 0

Fig. 6b,d is sketched in the occurrence of a magnetic field, and a denser streamline pattern is observed. This happens because the magnetic field generates a resistive force, which leads to a compression in the boundary layer region. Similarly, on increasing the shape parameter, the fluid slows down near the surface, which further compresses the streamlines. When a higher shape parameter along with the strong magnetic field is considered, streamlines observed are denser as observed in Fig. 6d. The study of these patterns may aid in the optimization systems involving MHD, including electromagnetic flow control, plasma confinement, and cooling systems.

5.2.3 Impact of m When χ = 0

Fig. 7a,c represents the absence of the porosity parameter, i.e., non-porous surface. It represents that the fluid can smoothly flow along the surface, leading to less compressed, smooth, and uniform streamlines. When porosity is absent, then the streamline pattern completely depends on the shape parameter. Enhancing the shape parameter often results in a thinner boundary layer, which leads to increased shear stress.

5.2.4 Impact of m When χ ≠ 0

Fig. 7b,d is sketched in the presence of the porosity parameter for different shape parameters. In the presence of a porosity parameter, additional complexity is developed in the flow, which leads to disruption in streamlines. With the porosity, the resistance in the flow decreases and spreads the streamlines, resulting in less dense streamlines. On the contrary, in the presence of both shape and porosity, more complex flow structures are observed.

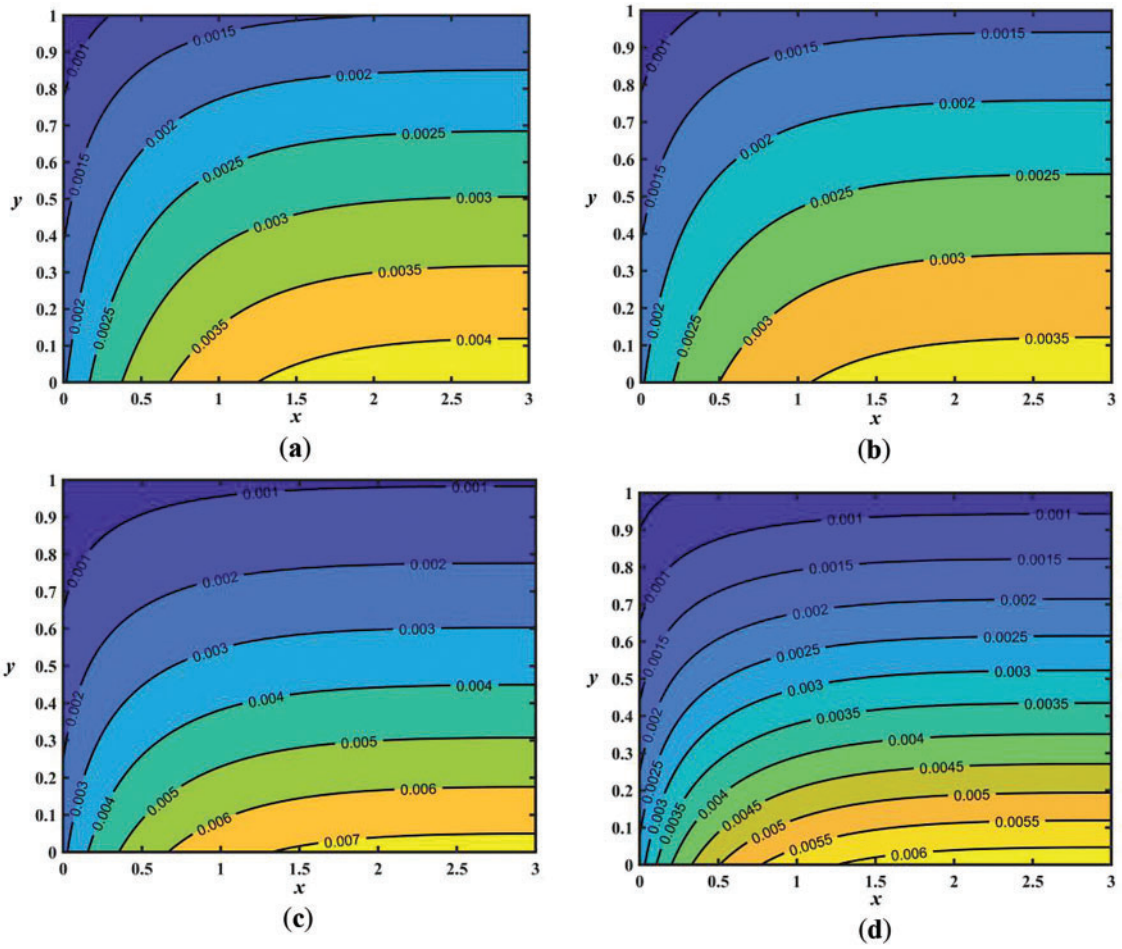

Figure 7: Effect of m and χ on streamlines. (a) $m = 0.5$, $\chi = 0$; (b) $m = 0.5$, $\chi = 2$; (c) $m = 2$, $\chi = 0$; (d) $m = 2$, $\chi = 2$

5.3 Impact of Magnetic Field

The impact of the magnetic field on the velocity and temperature profiles of the hybrid nanofluid are delineated in Figs. 8 and 9, respectively. When the *Mn* is applied on the flow, a resistive force is created due to the magnetic force exerted on nanoparticles of the hybrid nanofluid. This force is known as the Lorentz force. It is the combination of forces due to an electric field and magnetic field that results in a reduction in the velocity and can be visualized in Fig. 8. The drag force induced in the hybrid nanofluid results in frictional heating among nanoparticles, which is accountable for the temperature rise. This trend in the temperature can be seen in Fig. 9.

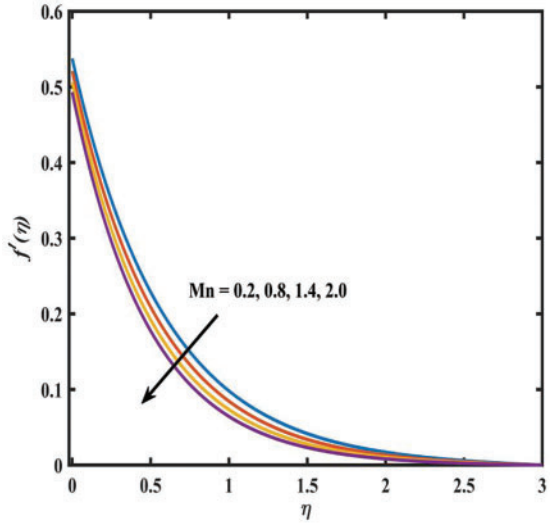

Figure 8: Effect of *Mn* on velocity

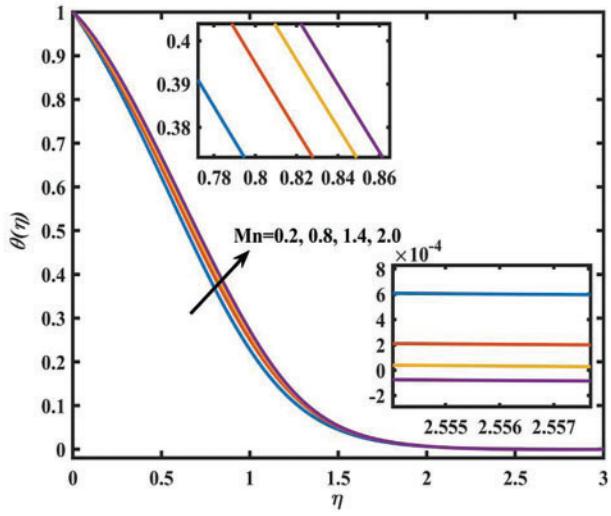

Figure 9: Effect of *Mn* on temperature

5.4 Impact of Velocity Slip Parameter

It defines the difference between the fluid's velocity and velocity at the boundary. It describes the drag between fluid and boundary. Fig. 10 delineates the velocity profile with the increment in the slip parameter. It shows the decrement in velocity with slip. The reason is the frictional drag, which is created due to the slip parameter. Fig. 11 is sketched to represent the effect of the slip variable on the temperature of the hybrid nanofluid. Initially, the temperature decreases, but later, it increases. The reason is that, at the initial stage, the thermal resistance is increased at the boundary, which results in reduced heat transfer efficiency, while later, with more increments in the slip parameter, convective heat transfer is enhanced, which results in an elevation in the thermal profile.

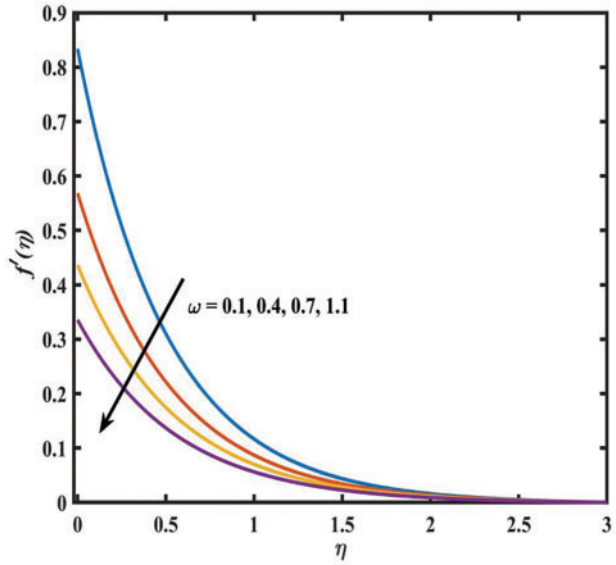

Figure 10: Effect of ω on velocity

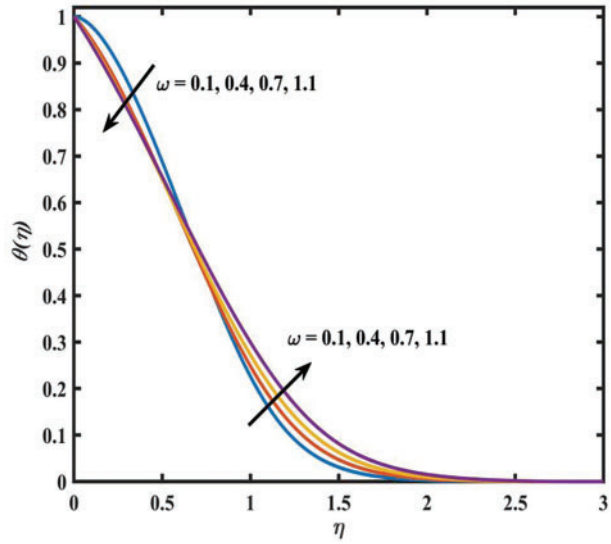

Figure 11: Effect of ω on temperature

5.5 Impact of Porosity Parameter

The porosity parameter generally describes the void space in the system. When the porosity is increased, the flow paths for the fluid become more complex, which improves the resistance in the flow, leading to a decrease in the velocity profile. This trend in velocity is delineated in Fig. 12. Due to a decrement in velocity, the kinetic energy of particles decreases, which lessens the convective heat transfer through the fluid particles. This results in a rise in the temperature of the fluid. The thermal outline is represented in Fig. 13.

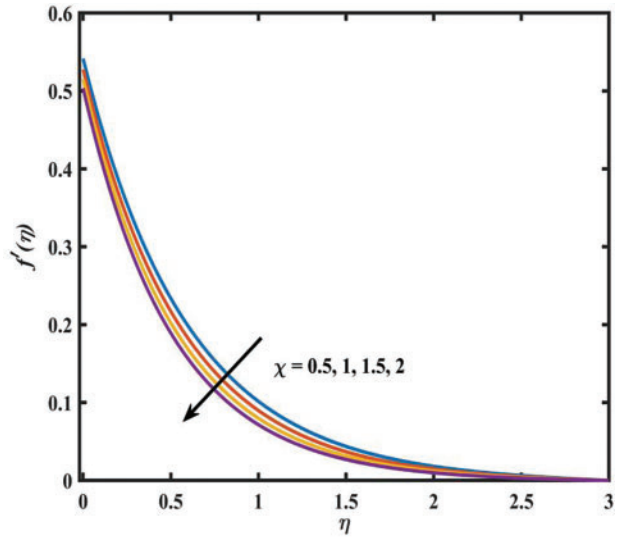

Figure 12: Effect of χ on velocity

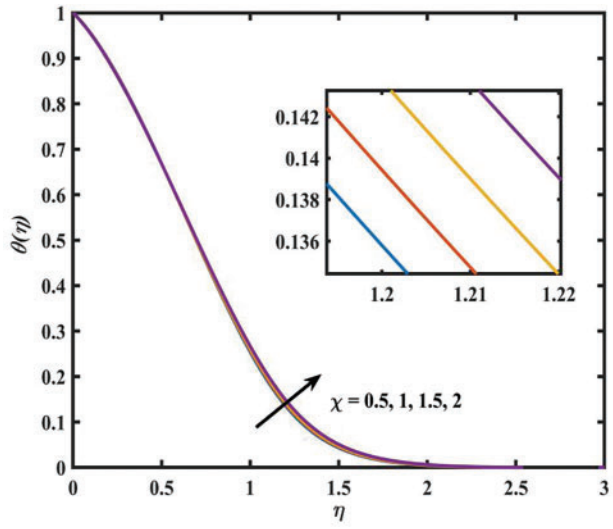

Figure 13: Effect of χ on temperature

5.6 Impact of Power Index Parameter

The power index parameter for a plate describes the variation in thickness. It generally describes how the thickness changes along the length or width of the plate. A larger power index parameter shows more surface area to the fluid. It leads to the increased drag on the fluid flow. This drag force is responsible for the reduced fluid's velocity, which is delineated in Fig. 14. The temperature profile due to the power index parameter is delineated in Fig. 15. It shows the dual behavior of the temperature profile. Initially, it is observed that the temperature of fluid decreases, but later, it increases. Initially, on increasing the power index parameter, the surface area in contact with the fluid increases, which enhances heat transfer away from the fluid, resulting in a decrease in temperature, while after

a restricted region, the thermal boundary layer develops. This results in a rise in temperature due to altered flow dynamics.

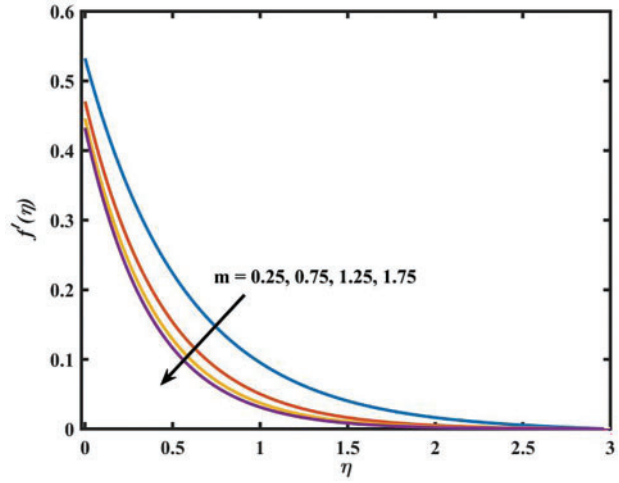

Figure 14: Effect of m on velocity

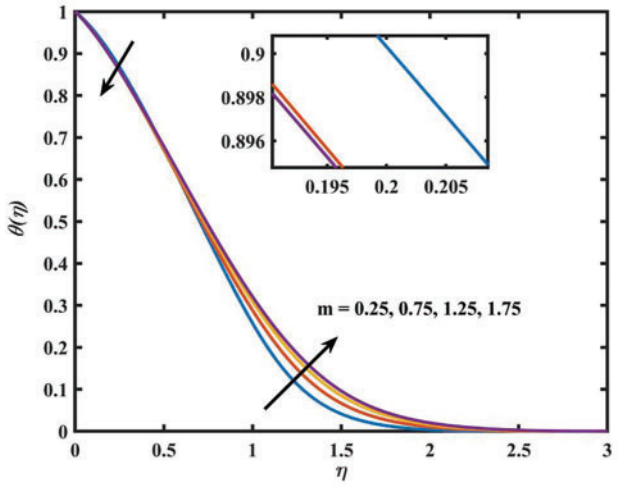

Figure 15: Effect of m on temperature

5.7 Impact of Mixed Convection Parameter

The mixed convection parameter (ζ) considers the combined effect of natural and forced convection. On rising the ζ, the natural convection becomes more significant, driven by buoyancy forces. These forces improve the fluid's motion, increasing the fluid's velocity. The trend is represented in Fig. 16. On the other hand, the cooling efficiency is improved due to the natural convection effect. The heat is easily transported to the surroundings, which leads to a decrement in the temperature profile. The trend in temperature can be observed in Fig. 17.

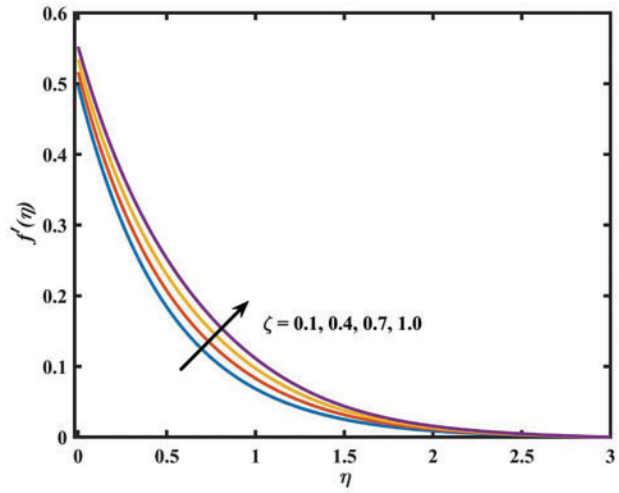

Figure 16: Effect of ζ on velocity

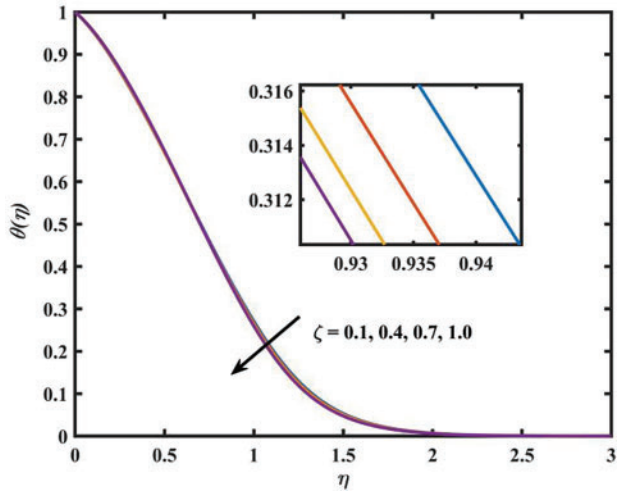

Figure 17: Effect of ζ on temperature

5.8 Local Nusselt Number Profiles

The Nusselt number describes the relation between convective and conductive heat transfer. A higher Nusselt number signifies a better convective heat transfer, which represents an efficient heat transfer from the surface to the fluid. Its understanding is essential for thermal management optimization.

5.8.1 Impact of Thickness Parameter

Fig. 18 delineates the impact of the thickness parameter on the heat transfer rate. It can be visualized that the local Nusselt number enhances with the increment in the thickness parameter. This is due to the increased surface area of the plate with a higher thickness parameter. This enhances the interaction between the plate and the fluid, leading to an advanced heat transfer rate.

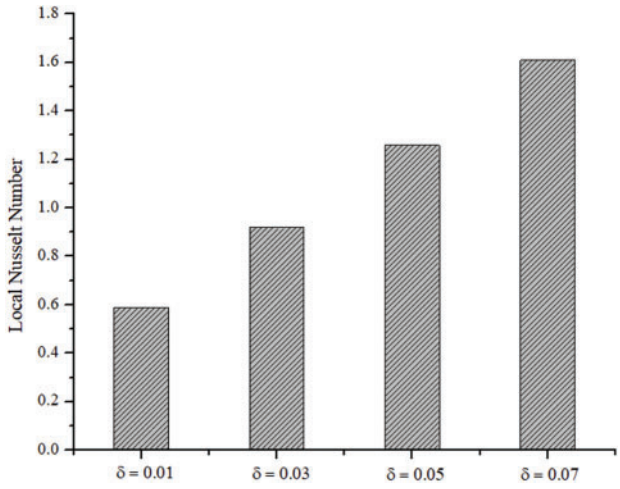

Figure 18: Effect of δ on local Nusselt number

5.8.2 Impact of Variable Thermal Conductivity Parameter

Fig. 19 is sketched to represent the consequence of ε on the local Nusselt number. It is detected that the heat transfer rate is decreased with the increment in the variable thermal conductivity parameter. Increased thermal conductivity means that the heat transfer in a fluid is due to molecular conduction rather than convection. Since the local Nusselt number explains the amount of heat transfer due to convection, compared to conduction, a higher value of the thermal conductivity parameter leads to a lower heat transfer rate.

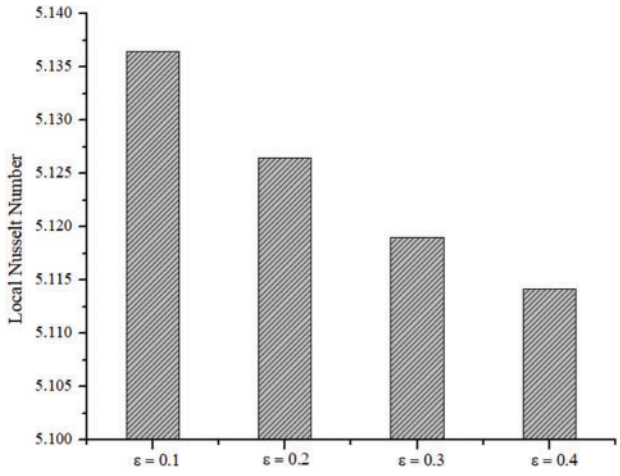

Figure 19: Effect of $\boldsymbol{\varepsilon}$ on local Nusselt number

6 Conclusions

In this work, the ANN technique is used for the assessment of the thermal behavior of TiO_2-Al_2O_3/kerosene oil flow over a porous non-flat plate. Moreover, for the study of changes in flow and

temperature field profiles, the impact of magnetohydrodynamics, mixed convection, velocity slip, and permeability variables are revealed. The major findings of this work are as:

- In the absence of porosity, the working fluid can smoothly flow along the surface, leading to less compressed, smooth, and uniform streamlines.
- The temperature of TiO_2-Al_2O_3/kerosene oil is constantly raised with an increase in the magnetic field.
- In the nonappearance of a magnetic field, the streamlines become a little dense on increasing the shape parameter.
- The dual nature of temperature outlines is observed with an increase in permeability.
- The velocity profiles are declined due to an upsurge in the values of the dimensionless variable Mn, ω, χ and m.
- The NN model predicts SFC and LNN values with an MSE of 0.0001367 and an overall R^2 value of 0.99841. The MSE value is near to zero, whereas the R^2 value is close to 1. It demonstrates the advantages of using an ANN model to analyze the heat transfer behavior of hybrid nanofluid flow over a non-flat plate with very low error and high prediction accuracy.

Given the significance of the problem under study, we can explore the following potential future research directions:

- As a general rule, fluids are not Newtonian. Consider some appropriate non-Newtonian fluid models instead of treating nanofluid as Newtonian. Moreover, the nano-encapsulated phase change material based on green nanofluids should be looked into.
- Instead of assuming a semi-infinite domain, further studies could consider a system where the upper surface has a variable thickness.
- The use of unsupervised learning techniques should be explored to obtain solutions to the solution governing equations.

Acknowledgement: The authors are thankful to all editors and reviewers for their valuable comments and suggestions.

Funding Statement: The authors received no specific funding for this study.

Author Contributions: The authors confirm contribution to the paper as follows: study conception and design: Himanshu Upreti, Alok Kumar Pandey; data collection: Himanshu Upreti; analysis and interpretation of results: Himanshu Upreti, Tanya Gupta; draft manuscript preparation: Alok Kumar Pandey. All authors reviewed the results and approved the final version of the manuscript.

Availability of Data and Materials: The data generated or analyzed in this research work are available from the corresponding author on reasonable request.

Ethics Approval: Not applicable.

Conflicts of Interest: The authors declare no conflicts of interest to report regarding the present study.

References

1. Turkyilmazoglu M, Pop I. Heat and mass transfer of unsteady natural convection flow of some nanofluids past a vertical infinite flat plate with radiation effect. Int J Heat Mass Transf. 2013;59:167–71. doi:10.1016/j.ijheatmasstransfer.2012.12.009.
2. Hatami M, Nouri R, Ganji DD. Forced convection analysis for MHD Al_2O_3–water nanofluid flow over a horizontal plate. J Mol Liq. 2013;187(5–6):294–301. doi:10.1016/j.molliq.2013.08.008.
3. Ahmadi AR, Zahmatkesh A, Hatami M, Ganji DD. A comprehensive analysis of the flow and heat transfer for a nanofluid over an unsteady stretching flat plate. Powder Technol. 2014;258(4):125–33. doi:10.1016/j.powtec.2014.03.021.
4. Das S, Mandal HK, Jana RN, Makinde OD. Magneto-nanofluid flow past an impulsively started porous flat plate in a rotating frame. J Nanofluids. 2015;4(2):167–75. doi:10.1166/jon.2015.1135.
5. Irfan M, Muhammad T, Rashid M, Anwar MS, Abas SS, Satya Narayana PV. Numerical study of nonlinear thermal radiation and Joule heating on MHD bioconvection Carreau nanofluid with gyrotactic microorganism's. J Radiat Res Appl Sci. 2025;18(1):101254. doi:10.1016/j.jrras.2024.101254.10.1016/j.jrras.2024.101254.
6. Shahlaei S, Hassankolaei MG. MHD boundary layer of GO-H_2O nanoliquid flow upon stretching plate with considering nonlinear thermal ray and Joule heating effect. Heat Trans Asian Res. 2019;48(8):4152–73. doi:10.1002/htj.21586.
7. Verma SK, Tiwari AK, Chauhan DS. Experimental evaluation of flat plate solar collector using nanofluids. Energy Convers Manag. 2017;134:103–15. doi:10.1016/j.enconman.2016.12.037.
8. Bazdidi-Tehrani F, Khabazipur A, Vasefi SI. Flow and heat transfer analysis of TiO_2/water nanofluid in a ribbed flat-plate solar collector. Renew Energy. 2018;122:406–18. doi:10.1016/j.renene.2018.01.056.
9. Tong Y, Lee H, Kang W, Cho H. Energy and exergy comparison of a flat-plate solar collector using water, Al_2O_3 nanofluid, and CuO nanofluid. Appl Therm Eng. 2019;159(1):113959. doi:10.1016/j.applthermaleng.2019.113959.
10. Saffarian MR, Moravej M, Doranehgard MH. Heat transfer enhancement in a flat plate solar collector with different flow path shapes using nanofluid. Renew Energy. 2020;146:2316–29. doi:10.1016/j.renene.2019.08.081.
11. Khademi R, Razminia A, Shiryaev VI. Conjugate-mixed convection of nanofluid flow over an inclined flat plate in porous media. Appl Math Comput. 2020;366(1):124761. doi:10.1016/j.amc.2019.124761.
12. Wahid NS, Md Arifin N, Khashi'ie NS, Pop I, Bachok N, Hafidzuddin MEH. MHD mixed convection flow of a hybrid nanofluid past a permeable vertical flat plate with thermal radiation effect. Alex Eng J. 2022;61(4):3323–33. doi:10.1016/j.aej.2021.08.059.
13. Khan U, Zaib A, Pop I, Abu Bakar S, Ishak A. Unsteady micropolar hybrid nanofluid flow past a permeable stretching/shrinking vertical plate. Alex Eng J. 2022;61(12):11337–49. doi:10.1016/j.aej.2022.05.011.
14. Thakur A, Sood S. Tri-hybrid nanofluid flow towards convectively heated stretching Riga plate with variable thickness. J Nanofluids. 2023;12(4):1129–40. doi:10.1166/jon.2023.1990.
15. Mandal G, Pal D. Dual solutions of radiative Ag-MoS_2/water hybrid nanofluid flow with variable viscosity and variable thermal conductivity along an exponentially shrinking permeable Riga surface: stability and entropy generation analysis. Int J Model Simul. 2024;44(6):360–85. doi:10.1080/02286203.2023.2171656.
16. Elsaid EM, AlShurafat KS. Impact of hall current and joule heating on a rotating hybrid nanofluid over a stretched plate with nonlinear thermal radiation. J Nanofluids. 2023;12(2):548–56. doi:10.1166/jon.2023.1927.
17. Bartwal P, Upreti H, Pandey AK, Joshi N, Joshi BP. Application of modified Fourier's law in a fuzzy environment to explore the tangent hyperbolic fluid flow over a non-flat stretched sheet using the LWCM approach. Int Commun Heat Mass Transf. 2024;153(11):107332. doi:10.1016/j.icheatmasstransfer.2024.107332.

18. Ermis K, Erek A, Dincer I. Heat transfer analysis of phase change process in a finned-tube thermal energy storage system using artificial neural network. Int J Heat Mass Transf. 2007;50(15–16):3163–75. doi:10.1016/j.ijheatmasstransfer.2006.12.017.
19. Popescu MC, Balas V, Perescu-Popescu L, Mastorakis N. Multilayer perceptron and neural networks. WSEAS Transac Circuits Syst. 2009;8(7):579–88.
20. Balachandar C, Arunkumar S, Venkatesan M. Computational heat transfer analysis and combined ANN-GA optimization of hollow cylindrical pin fin on a vertical base plate. Sadhana. 2015;40(6):1845–63. doi:10.1007/s12046-015-0403-5.
21. Hamdan MA, Abdelhafez EA, Hamdan AM, Haj Khalil RA. Heat transfer analysis of a flat-plate solar air collector by using an artificial neural network. J Infrastruct Syst. 2016;22(4):A4014004. doi:10.1061/(asce)is.1943-555x.0000213.
22. Verma TN, Nashine P, Singh DV, Singh TS, Panwar D. ANN: prediction of an experimental heat transfer analysis of concentric tube heat exchanger with corrugated inner tubes. Appl Therm Eng. 2017;120(3):219–27. doi:10.1016/j.applthermaleng.2017.03.126.
23. Naphon P, Wiriyasart S, Arisariyawong T, Nakharintr L. ANN, numerical and experimental analysis on the jet impingement nanofluids flow and heat transfer characteristics in the micro-channel heat sink. International J Heat Mass Transf. 2019;131:329–40. doi:10.1016/j.ijheatmasstransfer.2018.11.073.
24. Sharma RP, Madhukesh JK, Shukla S, Prasannakumara BC. Numerical and Levenberg-Marquardt backpropagation neural networks computation of ternary nanofluid flow across parallel plates with Nield boundary conditions. Eur Phys J Plus. 2023;138(1):63. doi:10.1140/epjp/s13360-023-03680-4.
25. Alklaibi AM, Mouli KVVC, Sundar LS. Heat transfer, and friction factor of Fe_3O_4–SiO_2/Water hybrid nanofluids in a plate heat exchanger: experimental and ANN predictions. Int J Therm Sci. 2024;195(3):108608. doi:10.1016/j.ijthermalsci.2023.108608.
26. Reddisekhar Reddy SR, Jakeer S, Sathishkumar VE, Basha HT, Cho J. Numerical study of TC4-NiCr/EG+Water hybrid nanofluid over a porous cylinder with Thompson and Troian slip boundary condition: artificial neural network model. Case Stud Therm Eng. 2024;53:103794. doi:10.1016/j.csite.2023.103794.
27. Ferdows M, Ahmed M, Bhuiyan MA, Bég OA, Çolak AB, Leonard HJ. Neural network and thermodynamic optimization of magnetized hybrid nanofluid dissipative radiative convective flow with energy activation2024;1(4):1–35. doi:10.1080/10407782.2024.2329312.
28. Raja MAZ, Shoaib M, Hussain S, Nisar KS, Islam S. Computational intelligence of Levenberg-Marquardt backpropagation neural networks to study thermal radiation and Hall effects on boundary layer flow past a stretching sheet. Int Commun Heat Mass Transf. 2022;130(1):105799. doi:10.1016/j.icheatmasstransfer.2021.105799.
29. Kumar P, Almeida F, Nagaraja B, Ajaykumar AR, Al-Mdallal Q. Neural network model using levenberg marquardt backpropagation algorithm for the Prandtl fluid flow over stratified curved sheet. IEEE Access. 2024;12(3):102242–60. doi:10.1109/ACCESS.2024.3422099.
30. Mandal DK, Biswas N, Manna NK, Gorla RSR, Chamkha AJ. Hybrid nanofluid magnetohydrodynamic mixed convection in a novel W-shaped porous system. Int J Numer Methods Heat Fluid Flow. 2023;33(2):510–44. doi:10.1108/HFF-03-2022-0163.
31. Pantokratoras A, Fang T. Sakiadis flow with nonlinear Rosseland thermal radiation. Phys Scr. 2013;87(1):015703. doi:10.1088/0031-8949/87/01/015703.
32. Fang T, Zhang J, Zhong Y. Boundary layer flow over a stretching sheet with variable thickness. Appl Math Comput. 2012;218(13):7241–52. doi:10.1016/j.amc.2011.12.094.
33. Khader MM, Megahed AM. Numerical solution for boundary layer flow due to a nonlinearly stretching sheet with variable thickness and slip velocity. Eur Phys J Plus. 2013;128(9):100. doi:10.1140/epjp/i2013-13100-7.

34. Elbashbeshy EMA, Emam TG, Abdel-wahed MS. Flow and heat transfer over a moving surface with nonlinear velocity and variable thickness in a nanofluid in the presence of thermal radiation. Can J Phys. 2014;92(2):124–30. doi:10.1139/cjp-2013-0168.
35. Acharya N, Bag R, Kundu PK. On the impact of nonlinear thermal radiation on magnetized hybrid condensed nanofluid flow over a permeable texture. Appl Nanosci. 2020;10(5):1679–91. doi:10.1007/s13204-019-01224-w.
36. Gangadhar K, Kumari MA, Chamkha AJ. EMHD flow of radiative second-grade nanofluid over a Riga plate due to convective heating: revised buongiorno's nanofluid model. Arab J Sci Eng. 2022;47(7):8093–103. doi:10.1007/s13369-021-06092-7.
37. Zainal NA, Nazar R, Naganthran K, Pop I. MHD flow and heat transfer of hybrid nanofluid over a permeable moving surface in the presence of thermal radiation. Int J Numer Meth Heat Fluid Flow. 2021;31(3):858–79. doi:10.1108/hff-03-2020-0126.
38. Masood S, Farooq M. Influence of thermal stratification and thermal radiation on graphene oxide-Ag/H_2O hybrid nanofluid. J Therm Anal Calorim. 2021;143(2):1361–70. doi:10.1007/s10973-020-10227-7.
39. Sandeep N, Ranjana B, Samrat SP, Ashwinkumar GP. Impact of nonlinear radiation on magnetohydrodynamic flow of hybrid nanofluid with heat source effect. Proceed Inst Mech Eng. 2022;236(4):1616–27. doi:10.1177/09544089211070667.
40. Waqas H, Farooq U, Liu D, Abid M, Imran M, Muhammad T. Heat transfer analysis of hybrid nanofluid flow with thermal radiation through a stretching sheet: a comparative study. Int Commun Heat Mass Transf. 2022;138(1):106303. doi:10.1016/j.icheatmasstransfer.2022.106303.
41. Vijay N, Sharma K. Entropy generation analysis in MHD hybrid nanofluid flow: effect of thermal radiation and chemical reaction. Numer Heat Transf Part B. 2023;84(1):66–82. doi:10.1080/10407790.2023.2186989.
42. Yahya AU, Siddique I, Jarad F, Salamat N, Abdal S, Hamed YS, et al. On the enhancement of thermal transport of Kerosene oil mixed TiO_2 and SiO_2 across Riga wedge. Case Stud Therm Eng. 2022;34(1):102025. doi:10.1016/j.csite.2022.102025.
43. Kierzenka J, Shampine LF. A BVP solver based on residual control and the Maltab PSE. ACM Trans Math Softw. 2001;27(3):299–316. doi:10.1145/502800.502801.
44. Irfan M, Anwar MS, Kebail I, Khan WA. Thermal study on the performance of Joule heating and Sour-Dufour influence on nonlinear mixed convection radiative flow of Carreau nanofluid. Tribol Int. 2023;188:108789. doi:10.1016/j.triboint.2023.108789.
45. Prasad KV, Vaidya H, Vajravelu K, Rashidi MM. Effects of variable fluid properties on MHD flow and heat transfer over a stretching sheet with variable thickness. J Mech. 2017;33(4):501–12. doi:10.1017/jmech.2016.101.